Tropopause Evolution in a Rapidly Intensifying Tropical Cyclone: A Static Stability Budget Analysis in an Idealized, Axisymmetric Framework

Patrick Duran[*] and John Molinari

University at Albany, State University of New York, Albany, NY

[*]*Corresponding author address:* Department of Atmospheric and Environmental Sciences, University at Albany, State University of New York, 1400 Washington Avenue, Albany, NY.

E-mail: pduran2008@gmail.com

ABSTRACT

Large changes in tropopause-layer static stability are observed during the rapid intensification (RI) of an idealized, axisymmetric tropical cyclone (TC). Over the eye, static stability near the tropopause decreases and the cold-point tropopause height rises by up to 4 km at the storm center. Outside of the eye, static stability increases considerably just above the cold-point tropopause, and the tropopause remains near its initial level.

A budget analysis reveals that the advection term, which includes differential advection of potential temperature and direct advection of static stability, is important throughout the upper troposphere and lower stratosphere. Within the eye, differential advection plays a particularly important role in destabilizing the layer near and above the cold-point tropopause. Outside of the eye, the upper-tropospheric outflow layer exports high potential temperature (θ) air from the eyewall to large radii in the upper troposphere. This increase in θ forces stabilization below the outfow jet and destabilization above. Vertical wind shear above and below the outflow maximum induces vertical gradients of turbulence, which also modify the vertical stability profile. Meanwhile, radiative heating tendencies at the top of the cirrus canopy generally act to destabilize the upper troposphere and stabilize the lower stratosphere. These turbulent and radiative processes combine to play an important role in the development of the strong stable layer immediately above the cold-point tropopause during RI.

1. Introduction

Using a high-resolution dropsonde dataset collected during the Tropical Cyclone Intensity Experiment (TCI; Doyle et al. 2017), Duran and Molinari (2018) observed dramatic changes in tropopause structure during the rapid intensification (RI) of Hurricane Patricia (2015). The goal of the present paper is to analyze the processes that might have produced the upper-tropospheric and lower-stratospheric fluctuations observed in Patricia using an idealized axisymmetric simulation.

After undergoing a remarkably rapid intensification (RI), Hurricane Patricia (2015) attained the strongest wind speed ever recorded in a tropical cyclone (TC) (Kimberlain et al. 2016; Rogers et al. 2017). TCI dropsonde observations collected during this RI period revealed dramatic changes in the cold-point tropopause height and upper-level static stability (Duran and Molinari 2018). In particular, when Patricia was at tropical storm intensity shortly before RI commenced, a strong inversion layer existed just above the cold-point tropopause. During the first half of the RI period, this inversion layer weakened throughout Patricia's inner core, with the weakening most pronounced over the developing eye. By the time the storm reached its maximum intensity of 95 m s^{-1}, the inversion layer over the eye had disappeared almost completely, which was accompanied by a greater than 1-km increase in the tropopause height. Meanwhile over the eyewall region, the static stability increased and the tropopause remained near its initial level.

Despite the importance of tropopause-layer thermodynamics in theoretical models of hurricanes (Emanuel and Rotunno 2011; Emanuel 2012), most observational studies of the upper-tropospheric structure of TCs are decades old[1]. Recently, however, Komaromi and Doyle (2017) found that stronger TCs tended to have a higher and warmer tropopause over their inner core than weaker TCs. Their results are consistent with the evolution observed over the inner core of Hur-

---

[1] An in-depth review of these papers can be found in Duran and Molinari (2018).

3

ricane Patricia, in which the tropopause height increased and the tropopause temperature warmed throughout RI (Duran and Molinari 2018).

An idealized simulation of a TC analyzed by Ohno and Satoh (2015) suggested that the development of an upper-level warm core near the 13-km level acted to decrease the static stability near the tropopause within the eye. During the early stage of development in their simulation, large static stability existed above 16 km at all radii (their Fig. 9c). However, after the storm's intensification, the static stability within the eye above 16 km was markedly smaller (their Fig. 10c). Although the mechanisms that might drive this static stability evolution have not been examined explicitly, it might be related to the development of an upper-tropospheric warm core within the eye.

Stern and Zhang (2013) described the development of the TC warm core using a potential temperature (θ) budget analysis. Although the warm anomaly in their simulation maximized in the mid-levels, they noted that a secondary warming maximum also existed in the 12-14-km layer. Radial and vertical advection both played important roles in this warm core development throughout RI, and subgrid-scale diffusion became particularly important during the later stage of RI. The warming of the upper troposphere by these advective and diffusive processes could decrease the vertical θ gradient, thereby contributing to a decrease in static stability near the tropoopause within the eye.

Outside of the eye, in the presence of cirrus clouds, vertical gradients of radiative heating also can modify the tropopause-layer static stability. Bu et al. (2014) noted the existence of a shallow region of diurnal-mean net radiative cooling at the top of the TC cirrus canopy (see their Figs. 5, 11). This shallow region of cooling could act to destabilize the layer just below the top of the cirrus canopy and stabilize the layer immediately above. If the top of the cirrus canopy lies close to the

tropopause, these radiative processes could contribute to a stabilization of the lower stratosphere, as was observed in Hurricane Patricia.

To our knowledge, the only paper that has examined explicitly the static stability evolution in a modeled TC is Kepert et al. (2016), but their analysis was limited to the boundary layer. The analysis herein is based upon that of Stern and Zhang (2013), except using a static stability budget similar to that of Kepert et al. (2016), with a focus on the upper-tropospheric and lower-stratospheric evolution during RI.

2. Model Setup

The numerical simulations were performed using version 19.4 of Cloud Model 1 (CM1) described in Bryan and Rotunno (2009). The equations of motion were integrated on a 3000-km-wide, 30-km-deep axisymmetric grid with 1-km horizontal and 250-m vertical grid spacing. The computations were performed on an f-plane at 15°N latitude, over a sea surface with constant temperature of 30.5°C, which matches that observed near Hurricane Patricia (2015; Kimberlain et al. 2016). Horizontal turbulence was parameterized using the Smagorinsky scheme described in Bryan and Rotunno (2009, pg. 1773), with a prescribed mixing length that varied linearly from 100 m at a surface pressure of 1015 hPa to 1000 m at a surface pressure of 900 hPa. Vertical turbulence was parameterized using the formulation of Markowski and Bryan (2016, their Eq. 6), using an asymptotic vertical mixing length of 100 m. A Rayleigh damping layer was applied outside of the 2900-km radius and above the 25-km level to prevent spurious gravity wave reflection at the model boundaries. Microphysical processes were parameterized using the Thompson et al. (2004) scheme, and radiative heating tendencies were computed every two minutes using the Rapid Radiative Transfer Model for GCMs (RRTMG) longwave and shortwave schemes (Iacono et al. 2008). The initial temperature and humidity field was horizontally homogeneous and deter-

5

mined by averaging all Climate Forecast System Reanalysis (CFSR) grid points within 100 km of Patricia's center of circulation at 18 UTC 21 October 2015. The vortex described in Rotunno and Emanuel (1987, their Eq. 37) was used to initialize the wind field, setting all parameters equal to the values used therein.

Although hurricanes simulated in an axisymmetric framework tend to be more intense than those observed in nature, the intensity evolution of this simulation matches reasonably well with that observed in Hurricane Patricia. After an initial spin-up period of about 20 hours, the modeled storm (Fig. 1, blue lines) began an RI period that lasted approximately 18 hours. After this RI, the storm continued to intensify more slowly until the maximum 10-m wind speed reached 89 m s^{-1} and the sea-level pressure reached its minimum of 846 hPa 81 hours into the simulation. Hurricane Patricia (red stars) exhibited a similar intensity evolution prior to its landfall, with an RI period leading to a maximum 10-m wind speed of 95 m s^{-1} and a minimum sea-level pressure of 872 hPa.

3. Budget Computation

The static stability can be expressed as the squared Brunt-Väisälä frequency:

$$N_m^2 = \frac{g}{T}\left(\frac{\partial T}{\partial z} + \Gamma_m\right)\left(1 + \frac{T}{R_d/R_v + q_s}\frac{\partial q_s}{\partial T}\right) - \frac{g}{1+q_t}\frac{\partial q_t}{\partial z}, \tag{1}$$

where g is gravitational acceleration, T is temperature, R_d and R_v are the gas constants of dry air and water vapor, respectively, q_s is the saturation mixing ratio, q_t is the total condensate mixing ratio, and Γ_m is the moist-adiabatic lapse rate:

$$\Gamma_m = g(1+q_t)\left(\frac{1 + L_v q_s/R_d T}{c_{pm} + L_v \partial q_s/\partial T}\right), \tag{2}$$

where L_v is the latent heat of vaporization and c_{pm} is the specific heat of moist air at constant pressure. In the tropopause layer, q_s, $\partial q_s/\partial T$, and $\partial q_t/\partial z$ approach zero. In this limiting case,

6

Eq. 1 reduces to:

$$N^2 = \frac{g}{\theta} \frac{\partial \theta}{\partial z},$$

(3)

where θ is the potential temperature.

To compute N^2, CM1 uses Eq. 1 in saturated environments and Eq. 3 in sub-saturated environments. For simplicity, however, only Eq. 3 will be employed for the budget computations throughout the entire domain[2].

Taking the time derivative of Eq. 3 yields the static stability tendency:

$$\frac{\partial N^2}{\partial t} = \frac{g}{\theta} \frac{\partial}{\partial z} \frac{\partial \theta}{\partial t} - \frac{g}{\theta^2} \frac{\partial \theta}{\partial z} \frac{\partial \theta}{\partial t},$$

(4)

where the potential temperature tendency, $\partial \theta / \partial t$, can be written, following Bryan (cited 2018):

$$\frac{\partial \theta}{\partial t} = -u \frac{\partial \theta}{\partial r} - w \frac{\partial \theta}{\partial z} + HTURB + VTURB + MP + RAD + DISS$$

(5)

Each term on the right-hand side of Eq. 5 represents a θ budget variable, each of which is output directly by the model every minute.

The first term on the right-hand side of Eq. 4 is larger than the second term throughout most of the tropopause layer (not shown). Consequently, the contribution of each of the terms in Eq. 5 to the N^2 tendency can be interpreted in light of a vertical gradient of each term.

Taking the vertical gradient of the first two terms on the right-hand side of Eq. 5 yields the time tendency of the vertical θ gradient due to horizontal and vertical advection[3]:

$$\left(\frac{\partial}{\partial t} \frac{\partial \theta}{\partial z} \right)_{adv} = -u \frac{\partial}{\partial r} \frac{\partial \theta}{\partial z} - w \frac{\partial}{\partial z} \frac{\partial \theta}{\partial z} - \frac{\partial u}{\partial z} \frac{\partial \theta}{\partial r} - \frac{\partial w}{\partial z} \frac{\partial \theta}{\partial z}.$$

(6)

The first two terms on the right-hand side of Eq. 6 represent advection of static stability by the radial and vertical wind, respectively. These terms act to rearrange the static stability field, but

---

[2]The validity of this approximation will be substantiated later in this section.

[3]These terms include the tendencies due to implicit diffusion in the fifth-order finite differencing scheme, which are separated from the advection terms in the CM1 version 19.4 budget output.

cannot strengthen or weaken static stability maxima or minima. The third and fourth terms on the right-hand side of Eq. 6 represent, respectively, the tilting of isentropes in the presence of vertical wind shear, and the stretching or squashing of isentropes by vertical gradients of vertical velocity. Since these terms involve velocity gradients, they can act to strengthen or weaken static stability maxima or minima through differential advection. Unless otherwise stated, any reference to "advection" in this paper indicates the sum of all of the terms in Eq. 6.

Returning to Eq. 5, HTURB and VTURB are the θ tendencies from the horizontal and vertical turbulence parameterizations, MP is the tendency from the microphysics scheme, RAD is the tendency from the radiation scheme, and DISS is the tendency due to turbulent dissipation. This equation neglects Rayleigh damping, since the entire analysis domain lies outside of the regions where damping is applied. Each term in Eq. 5 is substituted for $\partial\theta/\partial t$ in Eq. 4, yielding the contribution of each budget term to the static stability tendency. These terms are summed, yielding an instantaneous "budget change" in N^2 every minute. The budget changes are then averaged over 24-hour periods and compared to the total model change in N^2 over that same time period, i.e.:

$$\Delta N^2_{budget} = \frac{1}{\delta t} \sum_{t=t_0}^{t_0+\delta t} \left.\frac{\partial N^2}{\partial t}\right|_t \tag{7}$$

$$\Delta N^2_{model} = N^2_{t_0+\delta t} - N^2_{t_0} \tag{8}$$

$$Residual = \Delta N^2_{model} - \Delta N^2_{budget} \tag{9}$$

where t_0 is an initial time and δt is 24 hours.

Eqs. 7-9 are plotted for three consecutive 24-hour periods in Fig. 2. For this and all subsequent radial-vertical cross sections, a 1-2-1 smoother is applied once in the radial direction to eliminate $2\Delta r$ noise that appears in some of the raw model output and calculated fields. The left column of Fig. 2 depicts the model changes computed using Eq. 8, together with Eq. 1 in saturated environments and Eq. 3 in subsaturated environments. The center column depicts the budget changes

8

computed using Eq. 7 together with Eq. 3 throughout the entire domain. Thus, the left column includes the effect of moisture in the N^2 computations, whereas the center column neglects moisture. The right column depicts the residuals, computed using Eq. 9 (i.e. the left column minus the center column.) In every 24-hour period, the budget changes are nearly identical to the model changes, which is reflected in the near-zero residuals in the right column. This indicates that the budget accurately represents the model variability, which implies that the neglect of moisture in the budget computation introduces negligible error within the analysis domain[4].

In the tropopause layer, some of the budget terms are small enough to be ignored. To determine which of the budget terms are most important, a time series of the contribution of each of the budget terms in Eq. 5 to the tropopause-layer static stability tendency is plotted in Fig. 3. For this figure, each of the budget terms is computed using the method described in Section 3, except with 1-hour averaging intervals instead of 24-hour intervals. The absolute values of these tendencies are then averaged over the radius-height domain of the plots shown in Fig. 2 and plotted as a time series[5]. Advection (Fig. 3, red line) plays an important role in the mean tropopause-layer static stability tendency at all times, and vertical turbulence (Fig. 3, blue line) and radiation (Fig. 3, dark green line) also contribute significantly. The remaining three processes - horizontal turbulence, microphysics, and dissipative heating - are negligible everywhere outside of the eyewall, and do not play important roles in the mesoscale tropopause variability.

The preceding analysis indicates that, at all times, three budget terms dominate the tropopause-layer static stability tendency: advection, vertical turbulence, and radiation. Variations in the

---

[4]This is not the case in the lower- and mid-troposphere, where the residual actually exceeds the budget tendencies in many places, likely due to the neglect of moisture; thus we limit this analysis to the upper troposphere and lower stratosphere.

[5]It will be seeen in subsequent figures that each of the terms contributes both positively and negatively to the N^2 tendency within the analysis domain. Thus, taking an average over the domain tends to wash out the positive and negative contributions. To circumvent this problem, the absolute value of each of the terms is averaged.

magnitude and spatial structure of these terms drive the static stability changes depicted in Fig. 2; subsequent sections will focus on these variations and what causes them.

4. Results

a. Static stability evolution

The average N^2 over the first day of the simulation (Fig. 4a) indicates the presence of a weak N^2 maximum just above the cold-point tropopause. Over the subsequent 24 hours, during the RI period, the N^2 within and above this layer decreased within the 25-km radius (Fig. 4b). This decreasing N^2 corresponded to an increase in the tropopause height within the developing eye, maximized at the storm center. Outside of the eye, meanwhile, the tropopause height decreased over the eyewall region (25-60-km radius) and increased only slightly outside of the 60-km radius. In this outer region, the N^2 maximum just above the tropopause strengthened during RI. These trends continued as the storm's intensity leveled off in the 48-72-hour period (Fig. 4c). The tropopause height increased to nearly 21 km at the storm center and sloped sharply downward to 16.3 km on the inner edge of the eyewall, near the 30 km radius. Static stability outside of the eye, meanwhile, continued to increase just above the cold-point tropopause. This N^2 evolution closely follows that observed in Hurricane Patricia (2015; Duran and Molinari 2018, see their Fig. 4). The mechanisms that led to these N^2 changes will be investigated in the subsequent sections.

b. Static stability budget analysis

(i) 0-24 hours

The initial spin-up period was characterized by a steady increase of the maximum wind speed from 11 m s^{-1} to 22 m s^{-1} (Fig. 1a, blue line), an intensification rate that closely matched that of TC Patricia (Fig. 1a, red stars). The weakening of the lower-stratospheric static stability maximum

10

during this period is reflected in the total N^2 budget change over this time (Fig. 5a). The layer just above the cold-point tropopause was characterized by decreasing N^2 (purple shading), maximizing at the storm center. At and immediately below the tropopause, meanwhile, N^2 increased during this time period (green shading). Although these tendencies extended out to the 200-km radius, they were particularly pronounced at innermost radii. A comparison of the contributions of advection (Fig. 5b), vertical turbulence (Fig. 5c), and radiation (Fig. 5d) reveals that advection was the primary driver of the N^2 tendency during this period, acting to stabilize near and just below the tropopause and destabilize above. Although vertical turbulence acted in opposition to advection (i.e. it acted to stabilize regions that advection acted to destabilize), the magnitude of the advective tendencies was larger, particularly at the innermost radii. The sum of advection and vertical turbulence (Fig. 5e) almost exactly replicated the static stability tendencies above the tropopause. Radiative tendencies, meanwhile, (Fig. 5d) acted to destabilize the layer below about 16 km and stabilize the layer between 16 and 17 km. The sum of advection, vertical turbulence, and radiation (Fig. 5f) reproduced the total change in N^2 almost exactly.

(ii) 24-48 hours

During the RI period, the maximum wind speed increased from 22 m s^{-1} to 80 m s^{-1} (Fig. 1a). Over this time, N^2 within the eye generally decreased above 16 km and increased below (Fig. 6a), with the destabilization above 16 km maximizing near the level of the mean cold-point tropopause. These tendencies at the innermost radii were driven almost entirely by advection (Fig. 6b). Vertical turbulence (Fig. 6c) and radiation (Fig. 6d) contributed negligibly to the static stability tendencies in this region.

Outside of the eye, the N^2 evolution exhibited alternating layers of positive and negative tendencies. Near and above 18 km existed an upward-sloping region of decreasing N^2 that extended out

11

to the 180-km radius. In this region, neither vertical turbulence nor radiation exhibited negative N^2 tendencies; advection was the only forcing for this destabilization. Immediately below this layer, just above the cold-point tropopause, was a region of increasing N^2 that sloped upward from 17 km near the 30-km radius to just below 18 km outside of the 100-km radius. Advection and vertical turbulence both contributed to this positive N^2 tendency, with advection playing an important role below about 17.5 km and and turbulence playing an important role above. The sum of advection and turbulence (Fig. 6e) reveals two separate regions of increasing N^2 in the 17-18-km layer rather than one contiguous region. The addition of radiation to these two terms, however, (Fig. 6f) provides the link between these two regions, indicating that radiation also plays a role in strengthening the stable layer just above the tropopause. In the 16-17-km layer, just below the cold-point tropopause, a horizontally-extensive layer of destabilization also was forced by a combination of advection, vertical turbulence, and radiation. The sum of advection and vertical turbulence accounts for only a portion of the decreasing N^2 in this layer, and actually indicates forcing for stabilization near the 50-km radius and outside of the 130-km radius. Radiative tendencies overcome this forcing for stabilization in both of these regions to produce the radially-extensive region of destabilization observed just below the tropopause.

The sum of advection, vertical turbulence, and radiation (Fig. 6f) once again closely follows the observed N^2 variability, except in the eyewall region, where the neglect of latent heating and horizontal turbulence introduces some differences.

(iii) 48-72 hours

After the storm's maximum wind speed leveled off near 80 m s^{-1} (Fig. 1a), the magnitude of the static stability tendencies within the eye decreased to near zero (Fig. 7a). Outside of the eye, however, N^2 continued to decrease in the layer immediately surrounding the tropopause and in-

crease just above. The sum of advection and vertical turbulence (Fig. 7e) indicates that these two processes account for most of the destabilization near the tropopause and some of the stabilization near the 18-km altitude. Below the tropopause, however, these two terms provided strong forcing for stabilization that was not observed in the budget change (Fig. 7a). Radiation (Fig. 7d), which generally forced stabilization above 17 km and destabilization below, balanced out this forcing for stabilization in the upper troposphere. In the eyewall region (30-80-km radius), advection and vertical turbulence combined to force destabilization in the 17-18-km layer (Fig. 7e), which was not observed in the budget change (Fig. 7a). Radiation provided strong forcing for stabilization, which outweighed this effect and produced net stabilization in a portion of this region. Outside of the 80-km radius, both advection (Fig. 7b) and vertical turbulence (Fig. 7c) provided forcing for stabilization near and just above the 18-km level. The sum of the two terms (Fig. 7e) indicates increasing N^2 near the 18-km level everywhere outside of the 80-km radius, but this stabilization is slightly weaker in the 90-120-km radial band than the observed value. The addition of radiation (Fig. 7f) provided the extra forcing for stabilization required to account for the observed increase in N^2. Outside of the 120-km radius, the region of radiative forcing for stabilization sloped downward, and the increase in N^2 observed near 18 km can be explained entirely by a combination of advection and vertical turbulence.

5. Discussion

a. The role of advection

Advection played an important role in the tropopause-layer N^2 evolution at all stages of intensification, but for brevity, this section will focus only on the RI (24-48-hour) period. To investigate the advective processes more closely, the individual contributions of horizontal and vertical advection

13

during the RI period are shown in Fig. 8, along with the corresponding time-mean radial and verti-

cal velocities and θ. The N^2 tendencies due to the two advective components (Fig. 8a,b) exhibited

strong cancellation, consistent with flow that was nearly isentropic. There existed, however, a

large region near the tropopause in which the total advective tendency was nonzero (Fig. 6b).

These nonzero tendencies were related to the development of the TC's secondary circulation as

the storm intensified.

During the RI period, strong radial and vertical circulations developed near the tropopause

(Fig. 8c,d), which forced high-magnitude N^2 tendencies due to advection (Fig. 8a,b). A layer

of strong outflow formed at and below the tropopause during this period, with the outflow maxi-

mum (dashed cyan line) curving from the 14-km level at the 50-km radius to just below the 16-km

level outside of the 80-km radius (Fig. 8c). Notably, the N^2 tendency due to horizontal advection

(Fig. 8a) tended to switch signs at this line, with stabilization below the outflow maximum and

destabilization above. This is consistent with the outflow layer carrying air with increasingly large

θ from the eyewall to large radii as the storm intensified. This increase in θ maximized near the

outflow maximum, which acted to decrease $\partial\theta/\partial z$ above the outflow maximum and increase it be-

low. This mechanism is the same as that discussed in Trier and Sharman (2009), in which vertical

wind shear in the outflow layer of a mesoscale convective system modified the upper-tropospheric

static stability through differential advection of isentropes.

Meanwhile in the lower stratosphere, a thin layer of 2-4 m s^{-1} inflow developed a few hundred

meters above the tropopause, similar to that which was observed in Hurricane Patricia (2015;

Duran and Molinari 2018) and in previous modeling studies (e.g. Ohno and Satoh 2015; Kieu et al.

2016). Since the isentropes in this layer sloped slightly upward with radius (i.e. $\partial\theta/\partial r < 0$), this

inflow acted to import lower θ air from outer radii to inner radii. Since the negative θ tendencies

14

maximized at the level of maximum inflow, the layer below the inflow maximum destabilized and the layer above stabilized (Fig. 8a).

Curiously, horizontal advection contributed to the N^2 tendency everywhere within the eye, even though the mean radial velocity there was near zero. Close examination of the model output revealed that these tendencies were forced by advective processes associated with inward-propagating waves. Although the radial velocity perturbations induced by these waves averaged out to zero, the advective tendencies forced by the radial velocity perturbations did not. Additionally, when these waves reached r=0, a dipole of vertical velocity resulted, with ascent above and descent below. For reasons that remain unclear, the regions of ascent were more persistent than the regions of descent, which resulted in the mean ascent observed near r=0 above 17 km in Fig. 8d.

Vertical advection also played an important role in the tropopause-layer static stability evolution. Within the eye, subsidence dominated below 17 km, while mean ascent existed near the storm center above 17 km. Although the magnitude of the subsidence was larger at lower altitudes, $\partial\theta/\partial z$ was smaller there. Because $\partial\theta/\partial z$ was smaller, the subsidence at lower levels could not accomplish as much warming as the subsidence at higher levels in the eye, consistent with the results of Stern and Zhang (2013). As a result, vertical advection within the eye stabilized the layer below 16 km during RI.

Outside of the 27-km radius, ascent dominated the troposphere, while a 1-1.5-km-deep layer of descent existed immediately above the tropopause. These regions of ascent and descent converged just above the tropopause; this convergence acted to compact the isentropes in this layer and increase the static stability. Above the lower-stratospheric subsidence maximum, meanwhile, vertical advection decreased N^2. Below the tropopause, differential vertical advection increased N^2 within the eyewall region and also at larger radii above the vertical velocity maximum at larger

15

radii. Outside of the eyewall and below the vertical velocity maximum, meanwhile, differential vertical advection acted to decrease N^2.

Comparing the N^2 tendencies forced by horizontal (Fig. 8a) and vertical (Fig. 8b) advection to the total advective tendency seen in Fig. 6b reveals that horizontal advective tendencies dominated the troposphere, while vertical advective tendencies dominated the layer near and above the tropopause. Thus, tilting of isentropes in the vicinity of the upper-tropospheric outflow maximum appears to be the most important advective process governing the N^2 tendency in the troposphere, whereas convergence of vertical velocity appears to be the most important advective process near the tropopause.

b. The role of radiation

During the initial spin-up period (0-24 hours; Fig. 9a), convection was not deep enough to deposit large quantities of ice near the tropopause and create a persistent cirrus canopy. Due to the lack of ice particles, the radiative heating tendencies during this period (Fig. 9b) were relatively small and confined to the region above a few particularly strong, although transient, convective towers. During RI (24-48 hours), the eyewall updraft strengthened and a radially-extensive cirrus canopy developed near the tropopause (Fig. 9c). The enhanced vertical gradient of ice mixing ratio at the top of the cirrus canopy induced strong diurnal-mean radiative cooling near the tropopause (Fig. 9d). This cooling exceeded 0.6 K h^{-1} (14.4 K day^{-1}) in some places and sloped downward from the lower stratosphere into the upper troposphere, following the top of the cirrus canopy. A small radiative warming maximum also appeared outside of the 140-km radius below this region of cooling. These results broadly agree with those of Bu et al. (2014; see their Fig. 11a), whose CM1 simulations produced a 0.3 K h^{-1} diurnally-averaged radiative cooling at the top of the cirrus canopy and radiative warming within the cloud that maximized near the 200-km radius. This broad

16

region of radiative cooling acted to destabilize the layer below the cooling maximum and stabilize the layer above, which can be seen in Fig. 6d. The small area of net radiative heating outside of the 140-km radius enhanced the destabilization above 16 km in this region and produced a thin layer of stabilization in the 15-16-km layer.

After the TC's RI period completed (48-72 hours), strong radiative cooling remained near the tropopause at inner radii (Fig. 9f), sloping downward with the top of the cirrus canopy to below the tropopause at outer radii. Cooling rates exceeded 1 K h^{-1} (24 K day^{-1}) just above the tropopause between the 30- and 70-km radii. This value is more than three times the maximum cooling rate of 0.3 K h^{-1} observed by Bu et al. (2014), a difference that is a consequence of their larger vertical grid spacing compared to that used here, along with a contribution from differing radiation schemes. To compare our results to theirs, we ran a simulation identical to that described in Section 2, except using the NASA-Goddard radiation scheme and 625-m vertical grid spacing, to match those of Bu et al. (2014). This simulation produced a maximum 24-hour-average radiative cooling rate of 0.3 K h^{-1}, which agrees with that shown in Bu et al. (2014). Another simulation using 625-m vertical grid spacing and RRTMG radiation produced 24-hour-average cooling rates of up to 0.6 K h^{-1}. This suggests that vertical grid spacing smaller than 625 m is necessary to resolve properly the radiative cooling at the top of the cirrus canopy, and that the results can be quite sensitive to the radiation scheme used.

Meanwhile below the tropopause, time-mean radiative warming spread from 30- to 160-km radius within the cirrus canopy. The existence of radiative cooling overlying radiative warming in this region led to radiatively-forced destabilization at and below the tropopause, as was observed in Fig. 7d. Beneath the warming layer existed a region of forcing for stabilization, while a much stronger region of forcing for stabilization existed in the lower stratosphere, above the cooling maximum.

17

357   The results herein suggest that, after the cirrus canopy developed, radiative heating tendencies

358   considerably destabilized the upper troposphere and stabilized the lower stratosphere.

359   *c. The role of turbulent mixing*

360   Fig. 10 depicts the effect of turbulent mixing on the vertical θ profile of an initially stably-

361   stratified layer. At the initial time in this schematic, θ is assumed to increase with height at a

362   constant rate (Fig. 10, left panel). The imposition of turbulence (blue hatching) adjusts the θ

363   profile within the mixed layer toward a constant value equal to the mean value of that layer in

364   the initial state (Fig. 10, right panel). Just above and just below the mixed layer, however, the θ

365   profile remains undisturbed. Consequently, although turbulent mixing acts to decrease $\partial\theta/\partial z$ in

366   the layer in which it is occurring, it actually increases $\partial\theta/\partial z$ just below and just above the layer.

367   Vertical gradients of turbulent mixing like those depicted here are quite important, particularly on

368   the flanks of the upper-tropospheric outflow jet.

369   Two distinct maxima of vertical eddy diffusivity developed in the tropopause layer as the storm

370   intensified (Fig. 11). Comparison of these turbulent regions to the N^2 tendencies in Figs. 6c and

371   7c reveals that the layers in which vertical eddy diffusivity maximized corresponded to layers of

372   destabilization due to vertical turbulence. Just outside of these layers, however, vertical turbulence

373   acted to increase N^2. The large vertical gradient of vertical eddy diffusivity near the tropopause

374   played an important role in developing the lower-stratospheric stable layer during RI. These results

375   support the hypothesized role of turbulence in setting the outflow-layer θ stratification in Emanuel

376   and Rotunno (2011).

18

6. Conclusions

The simulated N^2 evolution shown herein closely matched that observed during the RI of Hurricane Patricia (2015). Three N^2 budget terms dominated in the upper troposphere and lower stratosphere: advection, radiation, and vertical turbulence. Advection dominated within the eye, where it provided forcing for destabilization. Radiation and vertical turbulence played particularly important roles in developing the strong N^2 maximum just above the cold-point tropopause during RI.

To put the N^2 variability observed near the tropopause into context, Fig. 12 depicts the model change in N^2 over the RI period (hours 24-48) from 0 to 21 km altitude, along with the vertical eddy diffusivity and the radiative heating rate. The largest changes in N^2 occurred in a relatively shallow layer immediately surrounding the tropopause (Fig. 12a). This shallow layer also contained the largest diurnally-averaged radiative heating tendencies found anywhere in the domain (Fig. 12c). Values of vertical eddy diffusivity larger than any found outside of the boundary layer also resided in the upper troposphere (Fig. 12b). The results herein suggest that this turbulence not only develops as a response to the presence of small static stability and large vertical wind shear, as discussed by Molinari et al. (2014) and Duran and Molinari (2016), but also can actively increase the static stability in highly localized regions just above and below the mixed layers.

Since two of the most important processes contributing to the N^2 variability are parameterized, and one (radiation) closely depends on yet another parameterized process (microphysics), the tropopause-layer N^2 variability could be quite sensitive to the assumptions inherent to the parameterizations used. A better understanding of the microphysical characteristics of the TC cirrus canopy, its interaction with radiation, and outflow-layer turbulence is critical to understanding the tropopause-layer N^2 evolution.

In this paper, all of the variables were averaged over a full diurnal cycle to eliminate the effects of diurnal variability and isolate the overall storm evolution. Diurnal variations in static stability near the tropopause are potentially of interest with respect to the tropical cyclone diurnal cycle, and will be the subject of future work.

References

Bryan, G. H., cited 2018: The governing equations for CM1. [Available online at http://www2. mmm.ucar.edu/people/bryan/cm1/cm1_equations.pdf].

Bryan, G. H., and R. Rotunno, 2009: The maximum intensity of tropical cyclones in axisymmetric numerical model simulations. *Mon. Wea. Rev.*, **137**, 1770–1789.

Bu, Y. P., R. G. Fovell, and K. L. Corbosiero, 2014: Influence of cloud-radiative forcing on tropical cyclone structure. *J. Atmos. Sci.*, **71**, 1644–1622.

Doyle, J. D., and Coauthors, 2017: A view of tropical cyclones from above: The Tropical Cyclone Intensity (TCI) Experiment. *Bull. Amer. Meteor. Soc.*, **98**, 2113–2134.

Duran, P., and J. Molinari, 2016: Upper-tropospheric low Richardson number in tropical cyclones: Sensitivity to cyclone intensity and the diurnal cycle. *J. Atmos. Sci.*, **73**, 545–554.

Duran, P., and J. Molinari, 2018: Dramatic inner-core tropopause variability during the rapid intensification of Hurricane Patricia (2015). *Mon. Wea. Rev.*, **146**, 119–134.

Emanuel, K., 2012: Self-stratification of tropical cyclone outflow. Part II: Implications for storm intensification. *J. Atmos. Sci.*, **69**, 988–996.

Emanuel, K., and R. Rotunno, 2011: Self-stratification of tropical cyclone outflow. Part I: Implications for storm structure. *J. Atmos. Sci.*, **68**, 2236–2249.

Iacono, M. J., J. S. Delamere, E. J. Mlawer, M. W. Shephard, S. A. Clough, and W. D. Collins, 2008: Radiative forcing by long-lived greenhouse gases: Calculations with the AER radiative transfer models. *J. Geophys. Res.*, **113 (D13103)**.

Kepert, J. D., J. Schwendike, and H. Ramsay, 2016: Why is the tropical cyclone boundary layer not "well mixed"? *J. Atmos. Sci.*, **73**, 957–973.

Kieu, C., V. Tallapragada, D.-L. Zhang, and Z. Moon, 2016: On the development of double warm-core structures in intense tropical cyclones. *J. Atmos. Sci.*, **73**, 4487–4506.

Kimberlain, T. B., E. S. Blake, and J. P. Cangialosi, 2016: Tropical cyclone report: Hurricane Patricia. National Hurricane Center. [Available online at www.nhc.noaa.gov].

Komaromi, W. A., and J. D. Doyle, 2017: Tropical cyclone outflow and warm core structure as revealed by HS3 dropsonde data. *Mon. Wea. Rev.*, **145**, 1339–1359.

Markowski, P. M., and G. H. Bryan, 2016: LES of laminar flow in the PBL: A potential problem for convective storm simulations. *Mon. Wea. Rev.*, **144**, 1841–1850.

Molinari, J., P. Duran, and D. Vollaro, 2014: Low Richardson number in the tropical cyclone outflow layer. *J. Atmos. Sci.*, **71**, 3164–3179.

Ohno, T., and M. Satoh, 2015: On the warm core of a tropical cyclone formed near the tropopause. *J. Atmos. Sci.*, **72**, 551–571.

Rogers, R. F., S. Aberson, M. M. Bell, D. J. Cecil, J. D. Doyle, J. Morgerman, L. K. Shay, and C. Velden, 2017: Re-writing the tropical record books: The extraordinary intensification of Hurricane Patricia (2015). *Bull. Amer. Meteor. Soc.*, **98**, 2091–2112.

Rotunno, R., and K. A. Emanuel, 1987: An air-sea interaction theory for tropical cyclones. Part II: Evolutionary study using a nonhydrostatic axisymmetric numerical model. *J. Atmos. Sci.*, **44**, 542–561.

Stern, D. P., and F. Zhang, 2013: How does the eye warm? Part I: A potential temperature budget analysis of an idealized tropical cyclone. *J. Atmos. Sci.*, **70**, 73–89.

Thompson, G., R. M. Rasmussen, and K. Manning, 2004: Explicit forecasts of winter precipitation using an improved bulk microphysics scheme. Part I: Description and sensitivity analysis. *Mon. Wea. Rev.*, **132**, 519–542.

Trier, S. B., and R. D. Sharman, 2009: Convection-permitting simulations of the environment supporting widespread turbulence within the upper-level outflow of a mesoscale convective system. *Mon. Wea. Rev.*, **137**, 1972–1990.
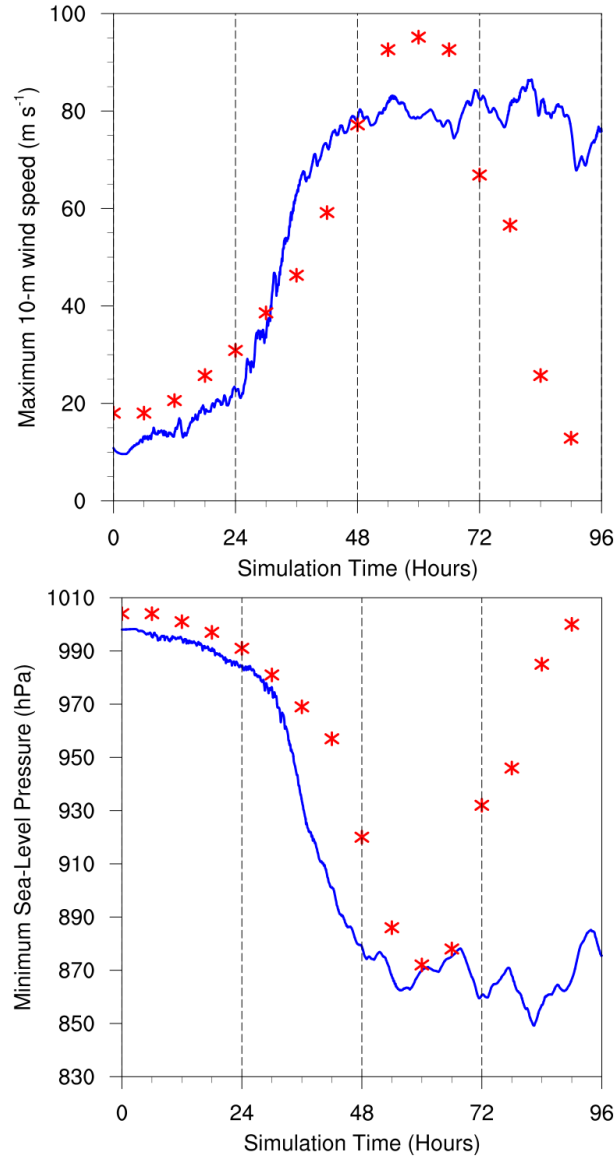
LIST OF FIGURES

23

FIG. 1. The maximum 10-m wind speed (top panel; m s^{-1}) and minimum sea-level pressure (bottom panel; hPa) in the simulated storm (blue lines; plotted every minute) and from Hurricane Patricia's best track (red stars; plotted every six hours beginning at the time Patricia attained tropical storm intensity). The rapid weakening during the later stage of Patricia's lifetime was induced by landfall.
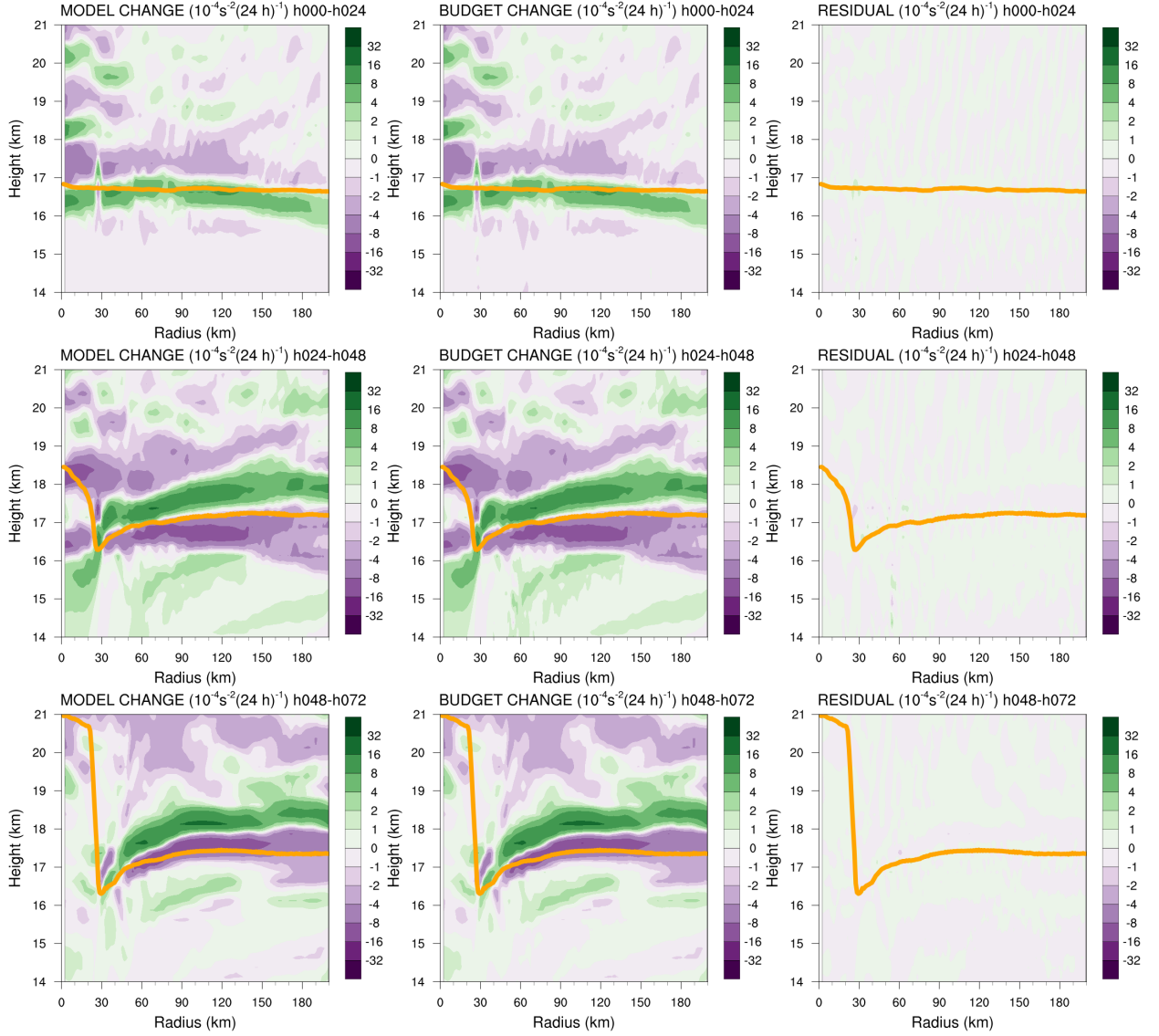
FIG. 2. Left panels: Twenty-four-hour changes in squared Brunt-Väisälä frequency (N^2; 10^{-4} s^{-2}) computed using Eq. 8 over (top row) 0-24 hours, (middle row) 24-48 hours, (bottom row) 48-72 hours. Middle Panels: The N^2 change over the same time periods computed using Eqs. 4-7, Right Panels: The budget residual over the same time periods, computed by subtracting the budget change (middle column) from the model change (left column). Orange lines represent the cold-point tropopause height averaged over the same time periods.
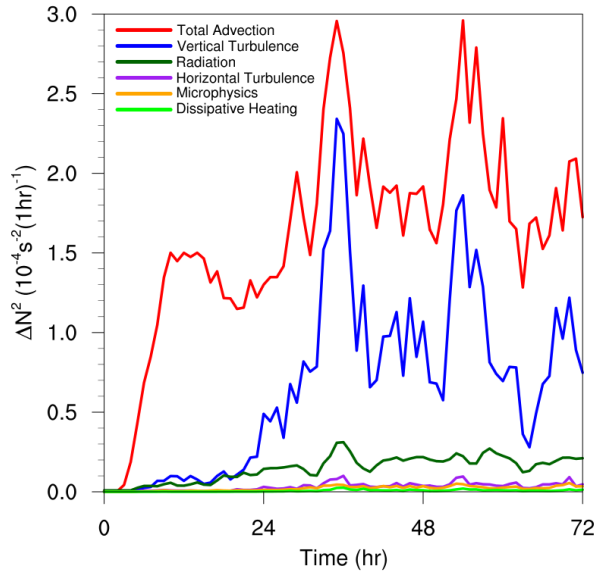
FIG. 3. Time series of the contribution of each of the budget terms to the time tendency of the squared Brunt-Väisälä frequency (N^2; 10^{-4} s^{-2}). For each budget term, the absolute value of the N^2 tendency is averaged temporally over 1-hour periods (using output every minute), and spatially in a region extending from 0 to 200 km radius and 14 to 21 km altitude.
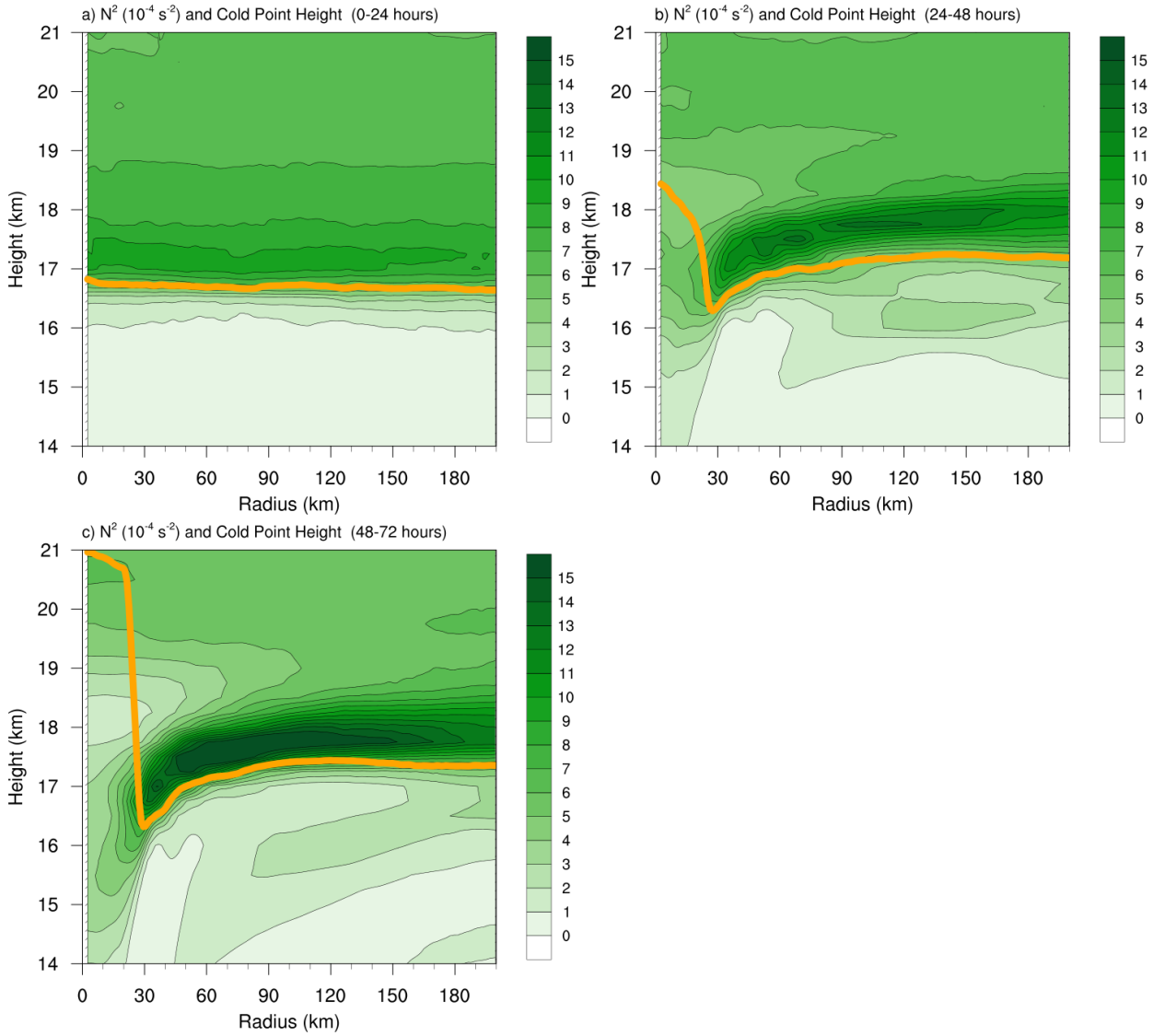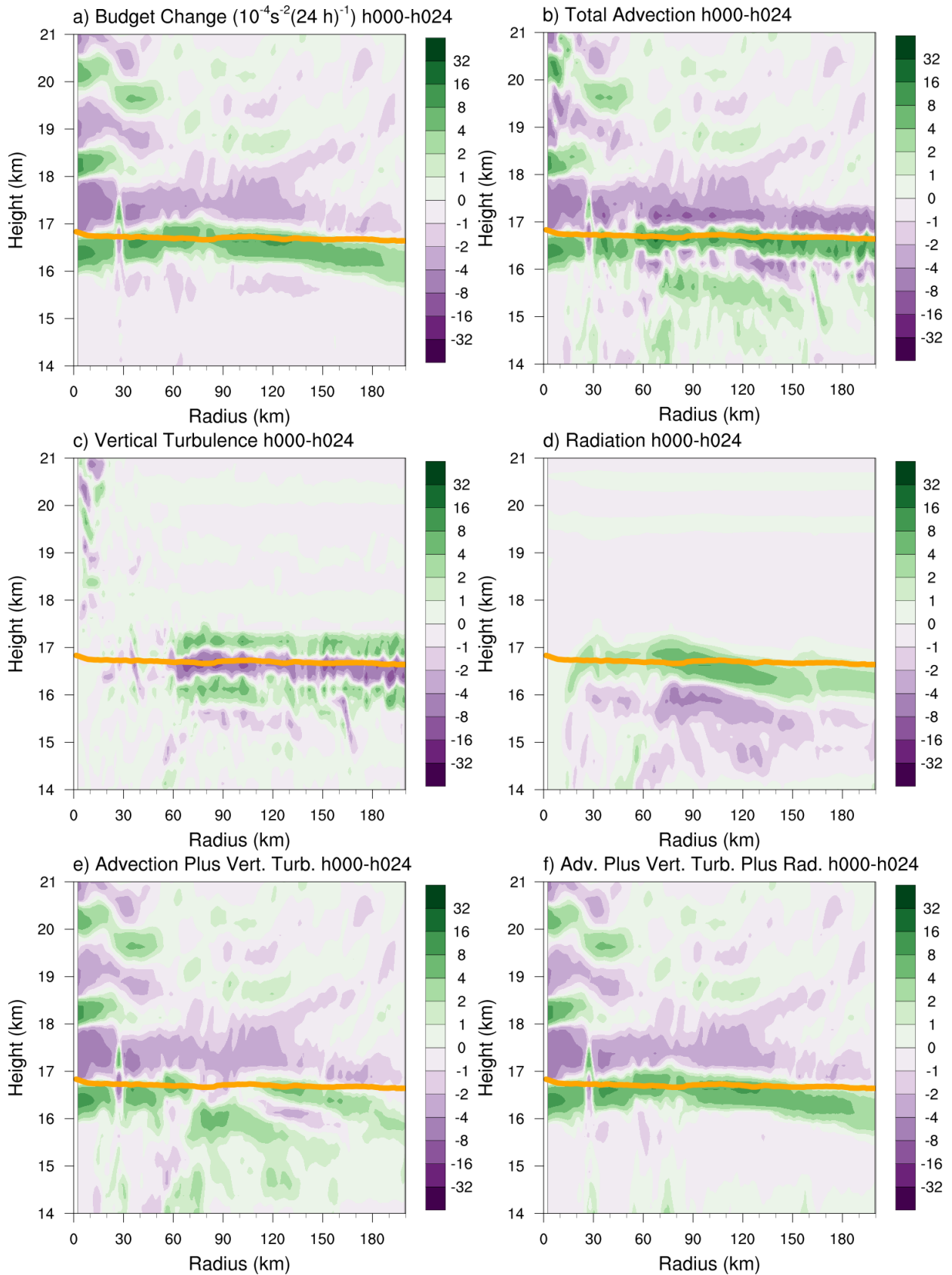
27

FIG. 4. Twenty-four-hour averages of squared Brunt-Väisälä frequency (N^2; 10^{-4} s^{-2}) over (a) 0-24 hours, (b) 24-48 hours, (c) 48-72 hours. Orange lines represent the cold-point tropopause height averaged over the same time periods.

a) Budget Change $(10^{-4}s^{-2}(24\ h)^{-1})$ h000-h024

b) Total Advection h000-h024

c) Vertical Turbulence h000-h024

d) Radiation h000-h024

e) Advection Plus Vert. Turb. h000-h024

f) Adv. Plus Vert. Turb. Plus Rad. h000-h024

FIG. 5. (a) Total change in N^2 over the 0-24-hour period (10^{-4} s^{-2} (24 h)$^{-1}$) and the contributions to that change from (b) the sum of horizontal and vertical advection, (c) vertical turbulence, (d) longwave and shortwave radiation, (e) the sum of horizontal advection, vertical advection, and vertical turbulence, and (f) the sum of horizontal advection, vertical advection, vertical turbulence, and longwave and shortwave radiation. Green shading indicates regions of stabilization and purple shading indicates regions of destabilization. Orange lines represent the cold-point tropopause height averaged over the 0-24-hour period.
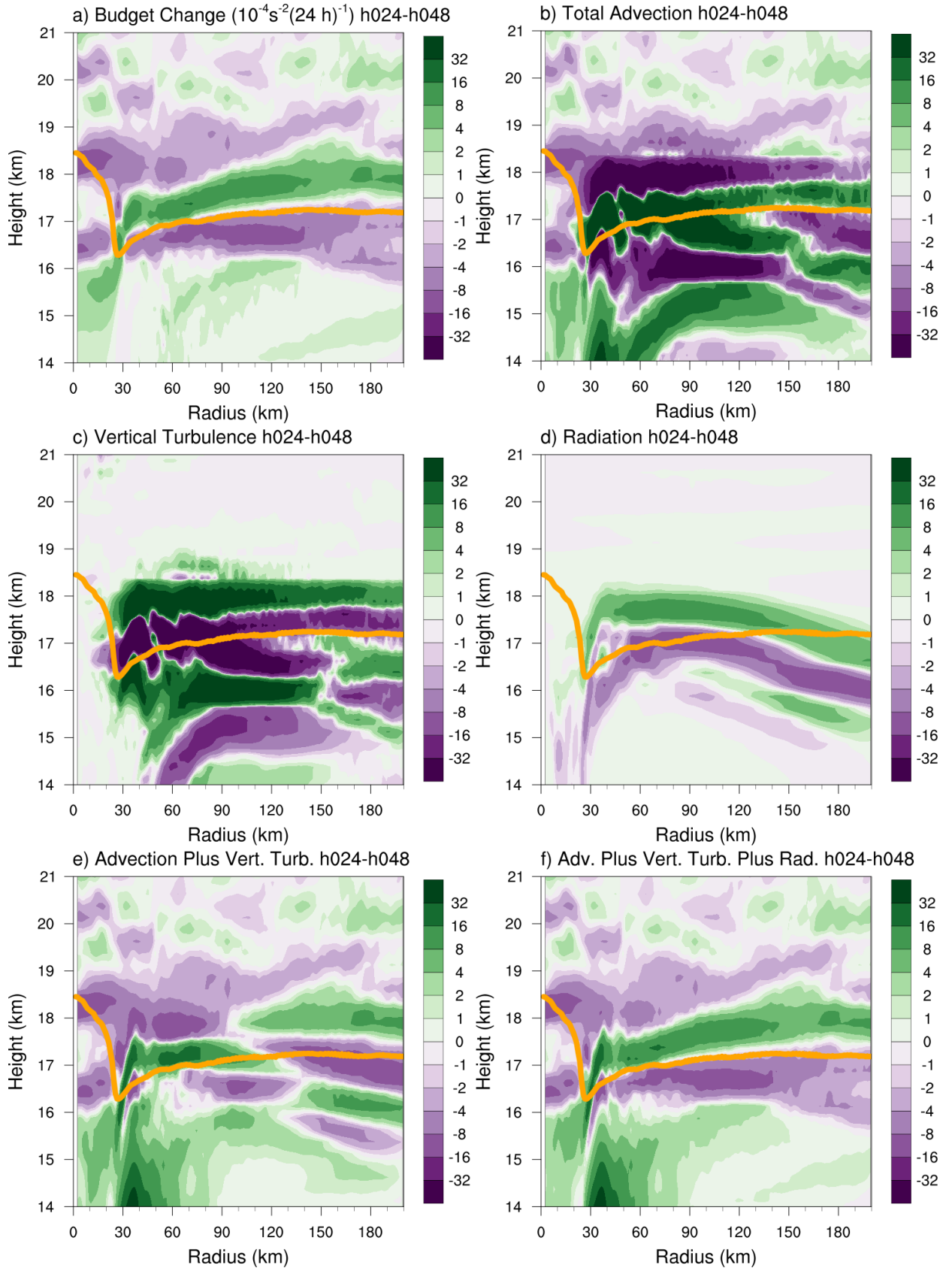
a) Budget Change $(10^{-4}s^{-2}(24\ h)^{-1})$ h024-h048

b) Total Advection h024-h048

c) Vertical Turbulence h024-h048

d) Radiation h024-h048

e) Advection Plus Vert. Turb. h024-h048

f) Adv. Plus Vert. Turb. Plus Rad. h024-h048
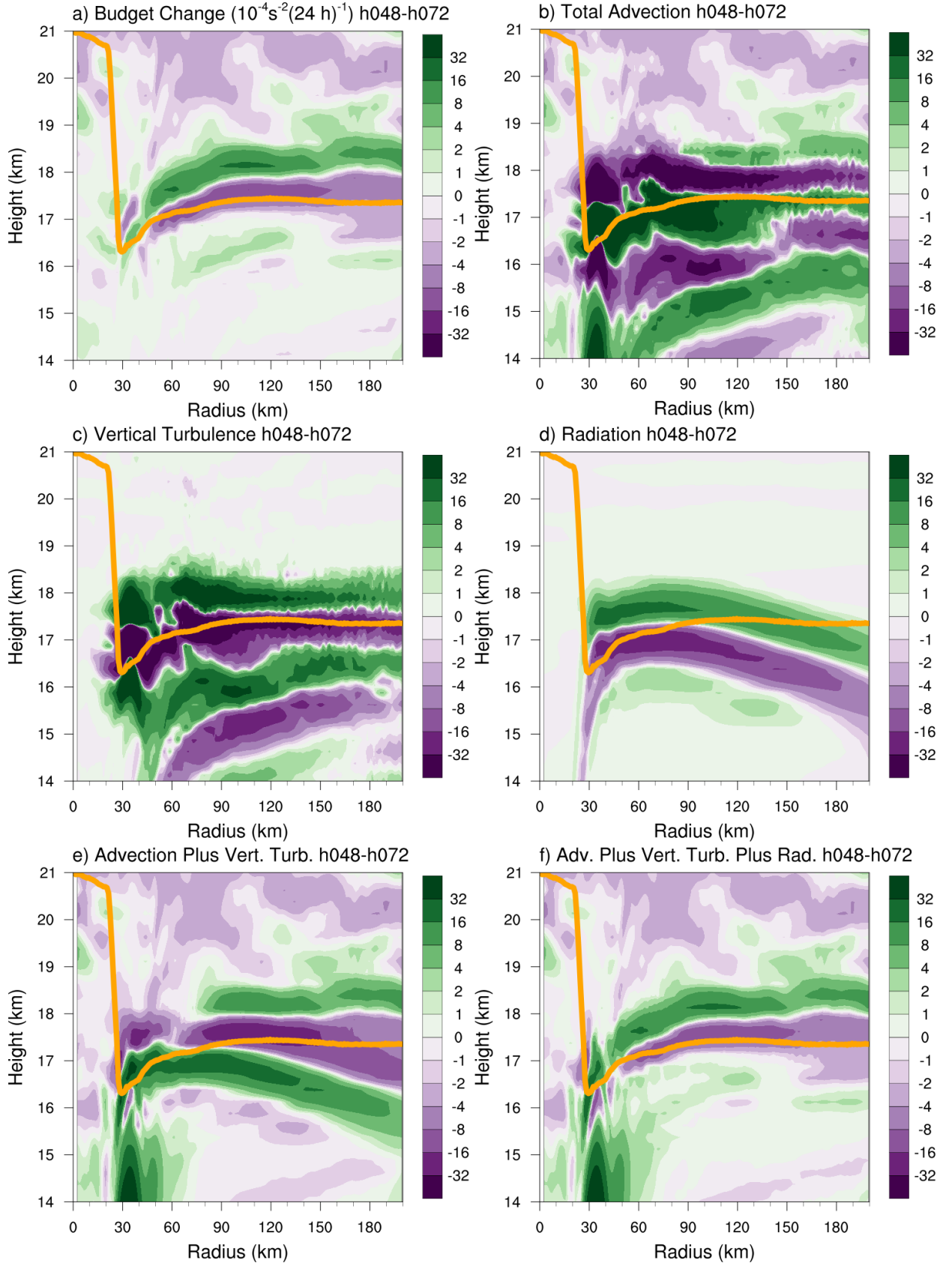
FIG. 6. As in Fig. 5, but for the 24–48-hour period.

31

FIG. 7. As in Fig. 5, but for the 48-72-hour period.
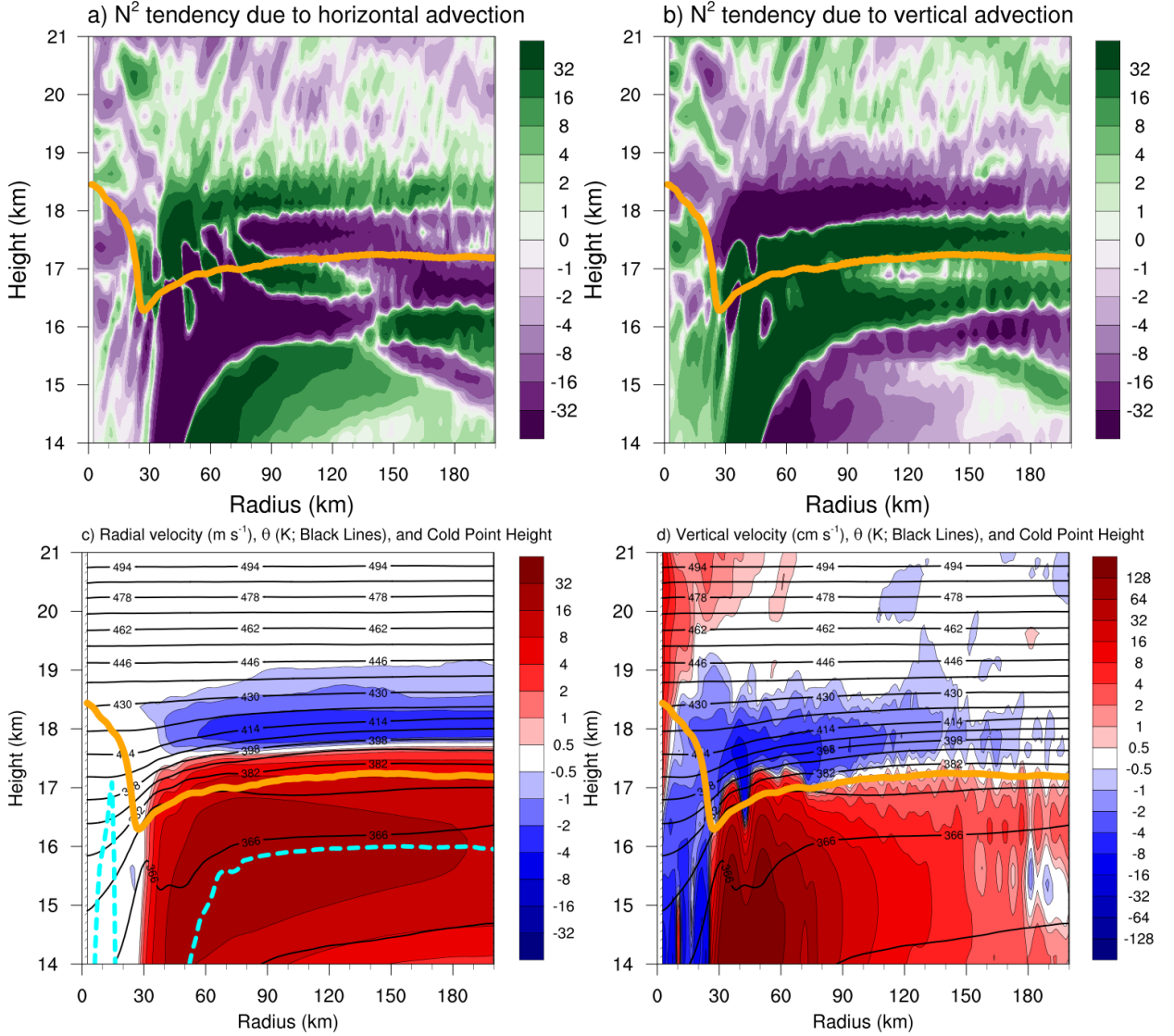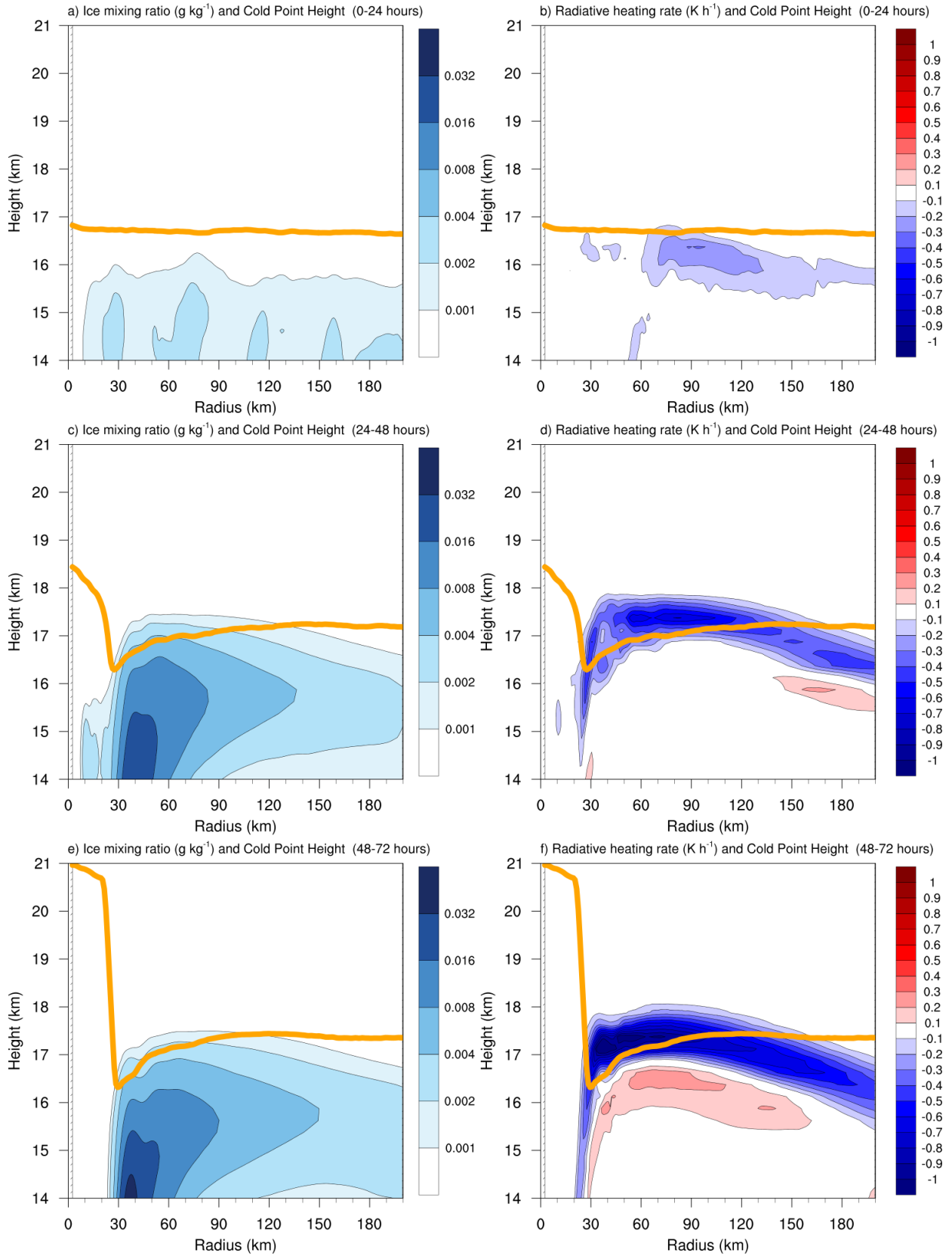
FIG. 8. The contributions to the change in N^2 over the 24-48-hour period (10^{-4} s^{-2} (24 h)$^{-1}$) by (a) horizontal advection and (b) vertical advection. (c) The radial velocity (m s^{-1}; filled contours), potential temperature (K; thick black contours), cold-point tropopause height (orange line), and level of maximum outflow (dashed cyan line) averaged over the 24-48-hour period. (d) The vertical velocity (cm s^{-1}; filled contours), potential temperature (K; thick black contours), and cold-point tropopause height (orange line) averaged over the 24-48-hour period.

33

a) Ice mixing ratio (g kg⁻¹) and Cold Point Height (0-24 hours)

b) Radiative heating rate (K h⁻¹) and Cold Point Height (0-24 hours)

c) Ice mixing ratio (g kg⁻¹) and Cold Point Height (24-48 hours)

d) Radiative heating rate (K h⁻¹) and Cold Point Height (24-48 hours)

e) Ice mixing ratio (g kg⁻¹) and Cold Point Height (48-72 hours)

f) Radiative heating rate (K h⁻¹) and Cold Point Height (48-72 hours)

₅₃₈ FIG. 9. Ice mixing ratio (g kg^{-1}) and cold-point tropopause height (orange lines) averaged over (a) 0-24 hours,

₅₃₉ (c) 24-48 hours, and (e) 48-72 hours. Radiative heating rate (K h^{-1}) and cold-point tropopause height (orange

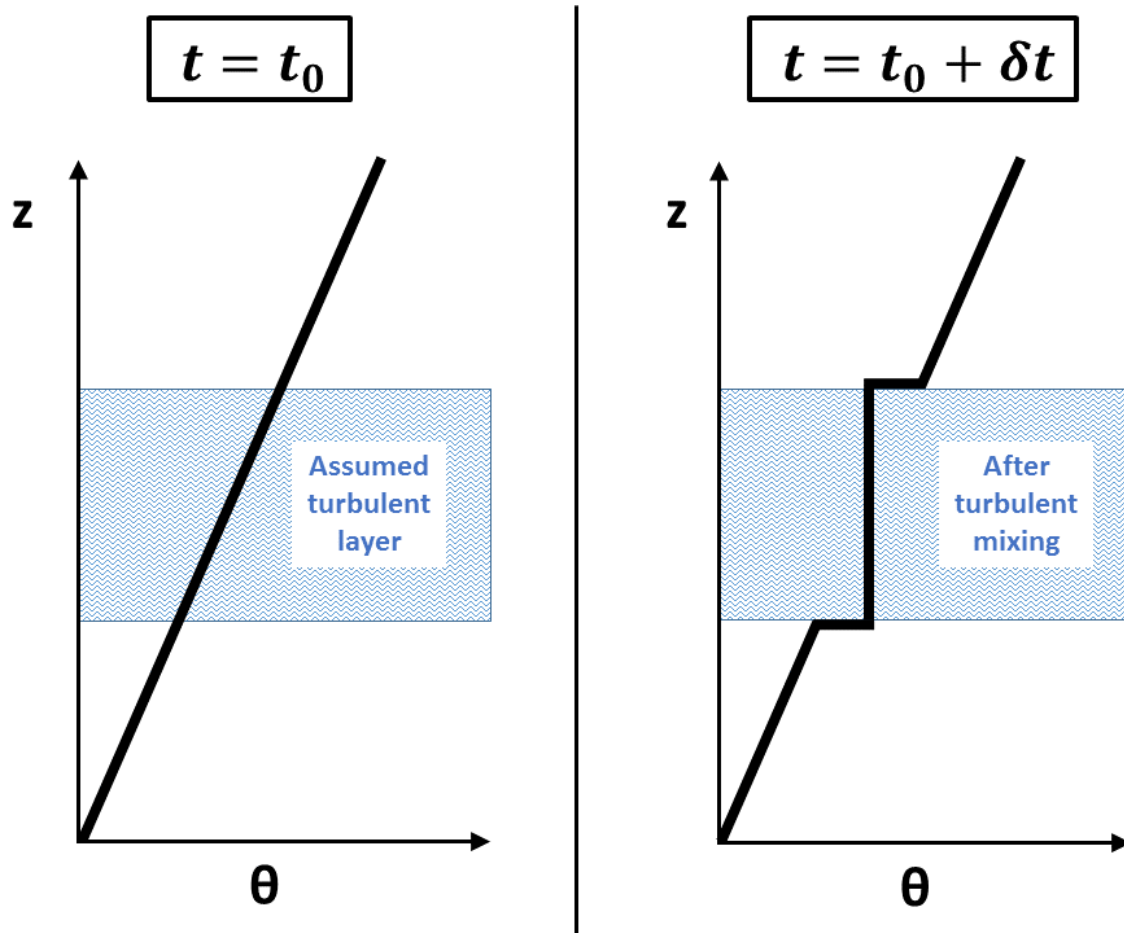₅₄₀ lines) averaged over (b) 0-24 hours, (d) 24-48 hours, and (f) 48-72 hours.

FIG. 10. Schematic diagram of the effect of turbulent mixing on the vertical profile of potential temperature (θ). At the initial time (left panel), potential temperature is assumed to increase with height at a constant rate (thick black line). The imposition of turbulence within a portion of the layer (blue hatching) adjusts the potential temperature profile toward the mean initial value of that layer. After a period of mixing (right panel) the potential temperature in the mixed layer does not vary with height, but just above and just below the mixed layer, it rapidly increases with height.
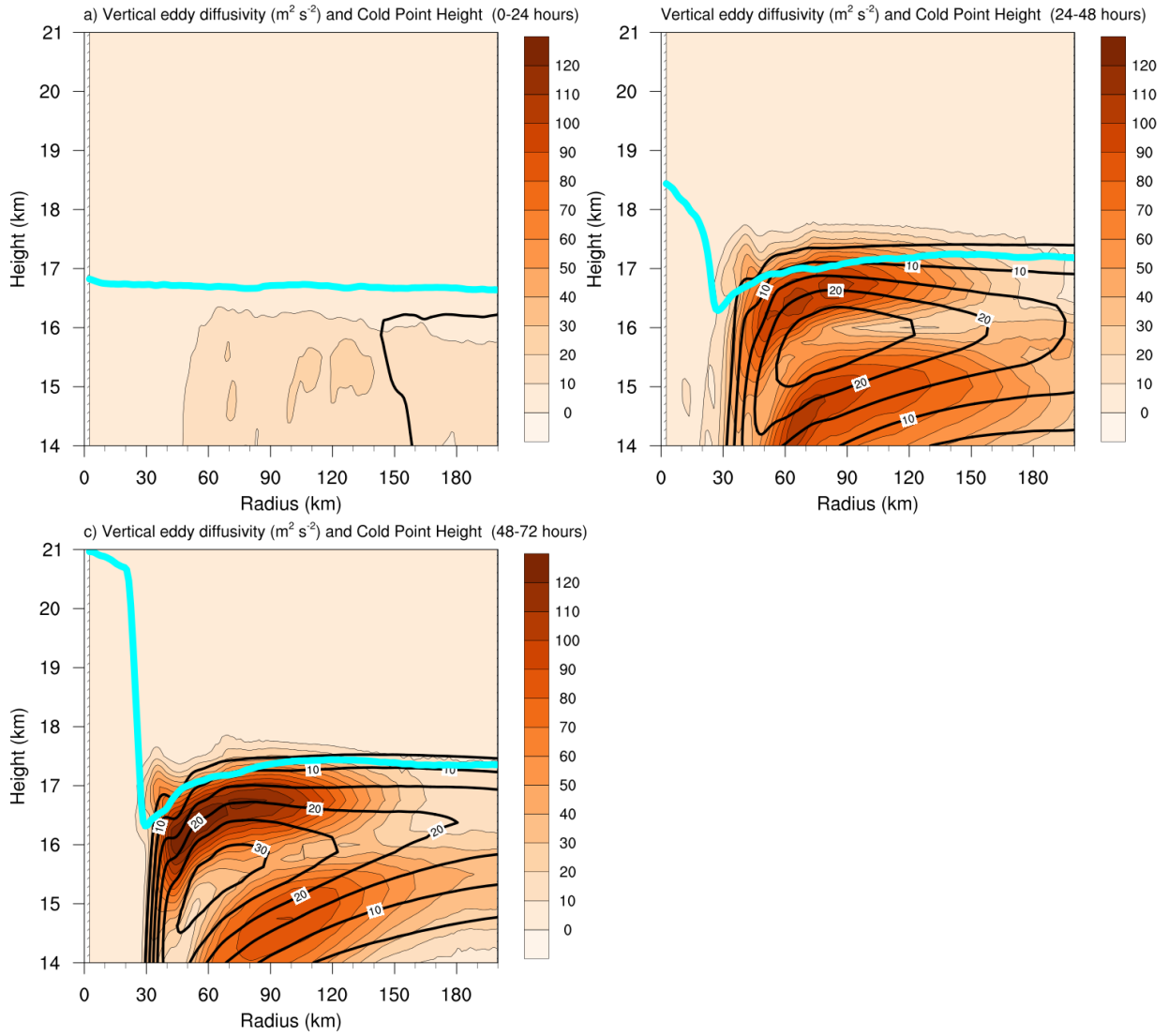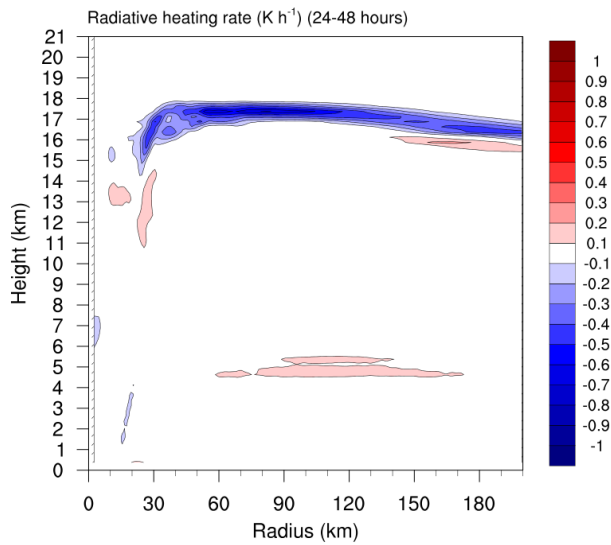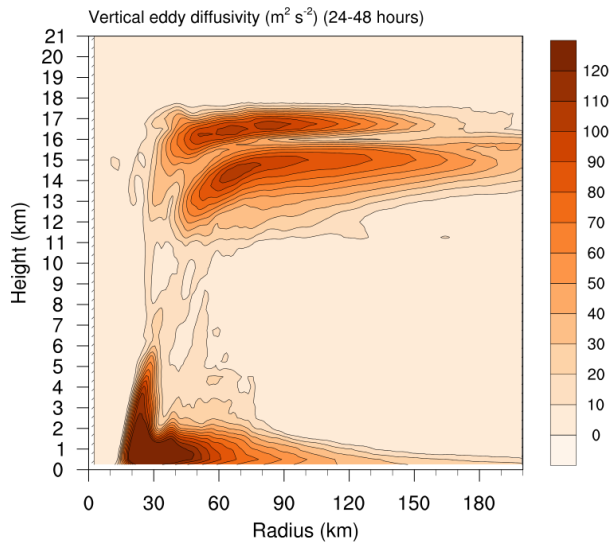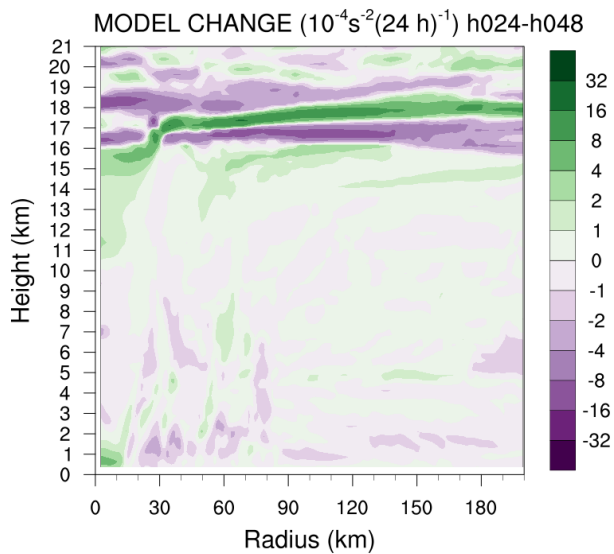
FIG. 11. Vertical eddy diffusivity (m^2 s^{-2}; filled contours), cold-point tropopause height (cyan lines), and radial velocity (m s^{-1}; thick black lines) averaged over (a) 0-24 hours, (b) 24-48 hours, and (c) 48-72 hours.

MODEL CHANGE $(10^{-4}\text{s}^{-2}(24\text{ h})^{-1})$ h024-h048

Vertical eddy diffusivity $(\text{m}^2\text{ s}^{-2})$ (24-48 hours)

Radiative heating rate (K h^{-1}) (24-48 hours)

549   FIG. 12. (Top panel) Change in N^2 over the 24-48-hour period (10^{-4} s^{-2} (24 h)$^{-1}$) directly output by the model

550   for the 0-21-km layer. (Middle panel) Vertical eddy diffusivity (m^2 s^{-2}) averaged over the same time period.

551   (Bottom panel) Radiative heating rate (K h^{-1}) averaged over the same time period.